Journal of Materials Chemistry C

ROYAL SOCIETY OF CHEMISTRY

PAPER

View Article Online
View Journal | View Issue



Cite this: J. Mater. Chem. C, 2025, 13, 18420

# *In situ* growth and ionic switching behavior of single-crystalline silver iodide nanoflakes†

Amir Parsi,[a] Abdulsalam Aji Suleiman,‡[a] Doruk Pehlivanoğlu,[a] Hafiz Muhammad Shakir,[b] Emine Yegin[a] and T. Serkan Kasırga *[a]

Received 2nd May 2025,
Accepted 22nd July 2025

DOI: 10.1039/d5tc01771h

rsc.li/materials-c

Silver iodide (AgI) is a prototypical superionic conductor, undergoing a first-order phase transition at 147 °C that enables rapid ionic transport through its lattice, making it attractive for solid-state ionic devices. However, due to the presence of mobile Ag ions, controlled chemical vapor deposition (CVD) synthesis of high-quality AgI single crystals has remained largely unexplored. Here, we present the controllable synthesis of thin, single-crystalline β-AgI nanoflakes using a home-built CVD setup with real-time optical observation capability, offering insights into their nucleation and growth dynamics. We evaluate the materials' environmental stability through temperature-dependent photodegradation and Ag nanoparticle formation induced by electron beam irradiation. Electrical measurements on two-terminal devices with silver contacts demonstrate a remarkable six-order-of-magnitude resistance drop in lateral configurations at elevated temperatures, indicative of switchable ionic conductivity. Additionally, vertical device architectures exhibit clear memristive (resistive switching) characteristics, likely due to the formation of conductive filaments. Our work addresses the key synthesis challenges and highlights the unique electrical properties of thin AgI single crystals, suggesting their potential for application in innovative devices based on unconventional computing, data storage, and advanced neuromorphic systems.



## 1. Introduction

Superionic conductors (SICs) are solid-state materials known for their high ionic conductivities, akin to those in molten salts, approximately 1 S $cm^{-1}$.[1,2] SICs often undergo an order–disorder transition to reach the superionic state, categorized into three classes based on the nature of the transition. Type I SICs, such as AgI, show a distinct first-order phase transition, while type II SICs, like $PbF_2$, show a continuous transition across the phases and type III SICs, like β-alumina, lack a well-defined transition.[1] These SICs possess high ionic conductivity, reflected in a diffusion coefficient $D$ of about $10^{-5}$ $cm^2$ $s^{-1}$, similar to how fast ions move in liquid water at room temperature.[1–3]

AgI has been an archetypal material to study type I SICs due to its peculiar properties and prospective applications.[2,4,5] It exhibits three polymorphs: body-centered cubic (α-AgI), hexagonal wurtzite (β-AgI), and cubic zinc blende (γ-AgI).[1,2,4,6–10] Below the critical temperature ($T_c$ = 147 °C), AgI exists in the low-conducting β and γ phases. At $T_c$, it undergoes a sharp solid-state phase transition to superionic α-AgI. During this transition, the iodine sublattice changes from a hexagonal close-packed (hcp) to a body-centered cubic (bcc) structure, while the silver sublattice shifts from an ordered to a disordered configuration. Below $T_c$, the silver ions are relatively immobile. Above this temperature, however, they exhibit a liquid-like behavior, hopping between tetrahedral sites within the iodine sublattice. This transition is considered to underlie the substantial ionic conductivity (~1 S $cm^{-1}$) observed in the α phase and the sharp, four-fold increase in conductivity at the critical temperature.[1,2,10] The conductivity remains relatively stable up to the melting point of 552 °C, after which it decreases slightly.[1,2,4,9]

In its three-dimensional (3D) form, AgI typically exhibits a direct band gap (~2.8 eV), making it appealing for various optics applications.[11] Lucking *et al.* theoretically demonstrated that AgI can retain structural stability even at the monolayer level.[12] Recently, the experimental realization of a polycrystalline AgI thin film was achieved through room-temperature adsorption of molecular iodine onto specific Ag substrates.[13,14] However, ionic conductivity studies are often limited by the use of polycrystalline samples, where randomly oriented grains and grain boundaries introduce scattering sites that obscure intrinsic transport mechanisms. These structural inhomogeneities complicate the interpretation of ionic

[a] Bilkent University UNAM – Institute of Materials Science and Nanotechnology, Ankara 06800, Türkiye. E-mail: kasirga@unam.bilkent.edu.tr
[b] Department of Physics, Bilkent University, Ankara 06800, Türkiye

† Electronic supplementary information (ESI) available. See DOI: https://doi.org/10.1039/d5tc01771h

‡ Current address: Department of Engineering Fundamental Sciences, Sivas University of Science and Technology, Sivas 58000, Türkiye.

transport behavior. In contrast, single-crystalline samples provide well-defined transport pathways, enabling more precise investigations into the fundamental mechanisms of ion conduction. Despite their advantages, synthesizing high-quality single crystals remains challenging, leading to a continued reliance on polycrystalline materials. To the best of our knowledge, there are no reports on the direct synthesis of thin single-crystalline AgI nanostructures.

To address these challenges, we report the controllable vapor-phase growth of thin, single-crystalline β-AgI using a confined-space CVD approach with real-time optical monitoring. This setup allows the direct visualization of nucleation and growth dynamics, providing insights into the nanoscale morphological evolution of AgI. The resulting nanoflakes exhibit uniform shape, high crystallinity, and well-defined thickness. We also assess the materials' environmental stability by examining their temperature-dependent photodegradation and the formation of Ag nanoparticles induced by electron beam irradiation. Finally, we demonstrate the impact of ionic transport in Ag-contacted two-terminal devices, revealing a six-order magnitude resistance drop in lateral configurations and memristive *I–V* characteristics in vertical structures.

## 2. Results and discussion

### 2.1. Real-time observation of AgI growth

AgI nanoflakes are grown using a home-built CVD setup that enables real-time optical observation (RTO) and synthesis control, as schematically depicted in Fig. 1a. Photographs of our setup are given in Fig. S1 (ESI†). The details of the RTO-CVD method can be found in earlier reports.[15–18] Small AgI granules are evenly distributed on mica loaded onto a substrate heater, after which a freshly cleaved mica, used as a growth substrate, is placed upside down on the AgI powder-loaded substrate to create a confined space configuration. Initially, the chamber is evacuated to 0.3 mbar and then purged with 100 sccm of high-purity argon gas (Ar) for 5 minutes to remove oxygen from the tube. The temperature is then increased to 400 °C at a ramp rate of 15 °C $min^{-1}$ and held for 5 minutes to facilitate the successful growth of AgI crystals. Once the crystals of the desired size are observed optically, the substrate heater is turned off to allow natural cooling to room temperature. Throughout the growth process, the carrier gas flow rate is maintained at 50 sccm. Video S1 in the ESI† provides a real-time visualization of the crystal growth process.

The growth mechanism of thin, single-crystalline AgI nanoflakes is based on a vapor–solid process, which begins with the sublimation of AgI powder. The vapor-phase species then diffuse toward the upper mica substrate, where they undergo surface adsorption followed by the lateral spreading of adatoms. This sequential process leads to the formation of well-defined AgI nanoflakes on the bottom surface of the top mica substrate.

As demonstrated in Video S1, ESI,† a gradual color contrast variation, due to optical interference, across different crystals is observed during growth, indicating changes in crystal thickness. The crystals that formed directly on top of the precursor on the growth substrate are larger and thicker, measured using

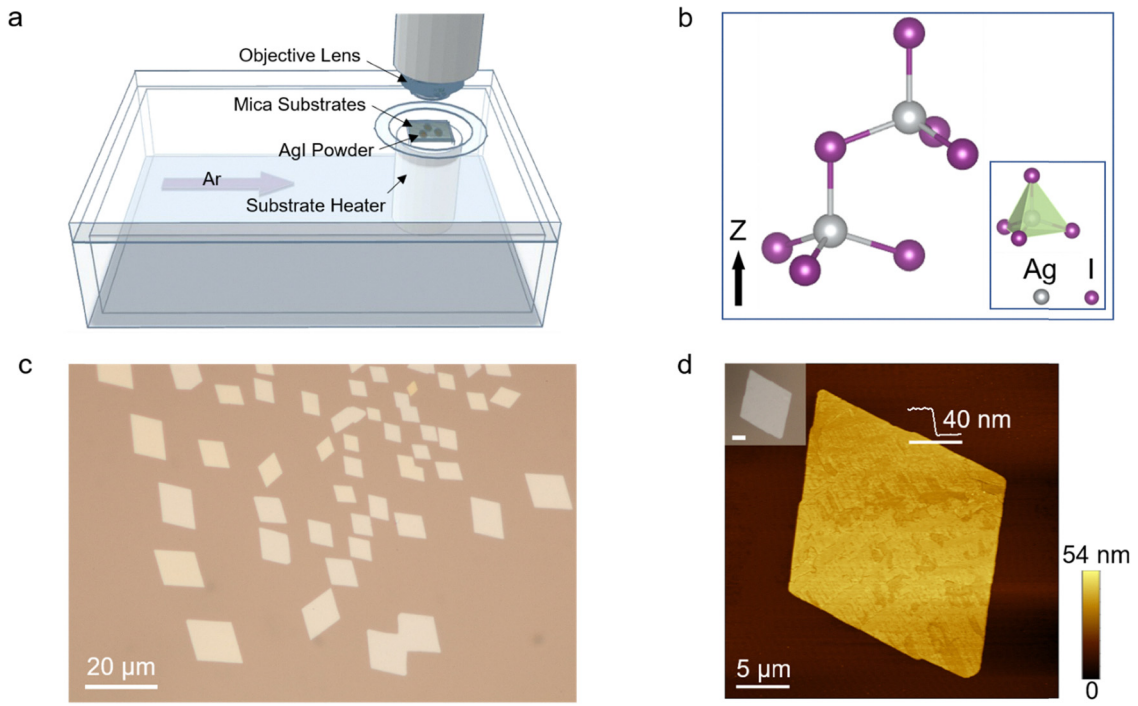


Fig. 1 (a) Schematic of the RTO-CVD chamber used to synthesize AgI crystals. (b) A schematic representation of the unit cell structure in the hexagonal form of β-AgI. (c) The optical micrograph of AgI nanoflakes grown on a mica substrate. (d) AFM height trace map of an as-grown nanoflake with a thickness of 40 nm. The corresponding optical microscopy image is shown in the inset. The scale bar is 5 μm.

an atomic force microscope (AFM) (Fig. S2, ESI†). Such a dramatic change in the crystal thickness in the vicinity of the precursor can be attributed to the nonuniform heat distribution around the precursor powder. Regions near the precursor are at higher temperatures as they are in direct contact with the precursor, making them a more favorable site for the adsorption of sublimated precursor molecules. The elevated temperature in this area boosts the adsorption rate of sublimated precursor molecules on the surfaces and edges of the nanoflakes as they grow.

A further increase in temperature above 420 °C leads to a decrease in the size and number of crystals. This can be attributed to a transition in the growth regime from adsorption-dominated to desorption-dominated kinetics. At elevated temperatures, adsorbed precursor species tend to desorb more rapidly from the substrate surface before they can contribute to nucleation and lateral growth, resulting in suppressed flake formation. Similar behavior has been observed in CVD growth of other materials such as $MoS_2$ and $HfO_2$, where excessive temperatures lead to a decline in nucleation density due to the enhanced desorption and surface diffusion effects.[19,20]

### 2.2. AgI characterization

We utilized optical, scanning electron, and atomic force microscopy to characterize the synthesized nanoflakes. Fig. 1b shows the schematic representation of the unit cell for the hexagonal structure of β-AgI, composed of two $[AgI_4]$ clusters.[11,13,21] Fig. 1c represents the optical micrograph of typical AgI nanoflakes synthesized on a mica substrate using RTO-CVD. As shown in Fig. 1d, the AFM height trace maps of the AgI crystal reveal a 40 nm thick nanoflake possessing a rhomboidal-shaped morphology with sharp edges. The nanoflakes can grow as large as several tens of micrometers in the lateral direction.

Although the as-synthesized crystals are often described as air-sensitive, our observations show that they remain stable under ambient conditions when protected from intense light exposure and elevated temperatures. Specifically, optical micrographs taken two months after synthesis reveal no visible signs of degradation in samples stored in air but shielded from direct illumination. These long-term images (Fig. S3a and b, ESI†) indicate that the nanoflakes largely retain their original morphology and surface features compared to their as-grown state. Raman spectroscopy performed on the same samples confirms that the characteristic vibrational modes of β-AgI remain largely unchanged, suggesting the preservation of the crystal structure over time (Fig. S3c, ESI†).

However, the crystals exhibit pronounced photo-induced degradation, particularly at elevated temperatures. This degradation is not driven by oxidation involving atmospheric oxygen, as it also occurs under inert Ar gas flow. Instead, it is attributed to light-induced reduction processes. For instance, if the optical microscope light remains on during the cooling period in CVD growth, degradation occurs in the illuminated areas despite the inert atmosphere (Fig. S4, ESI†). A similar effect is also observed when samples are illuminated under a microscope while being heated to 70 °C, 120 °C, 140 °C, and 170 °C (Fig. S5, ESI†), with degradation becoming significantly more severe above a certain temperature threshold. In contrast, regions not exposed to light show no signs of degradation, even at elevated temperatures. The dots observed on the surface of the crystals are Ag nanoparticles, likely formed due to the photo-induced breaking of bonds between iodine and silver. This bond-breaking leads to the removal of the iodine sublattice at high temperatures.[21] These results indicate that AgI crystals should be kept in the dark, especially during high-temperature studies, to prevent Ag island formation.

Additionally, we employed Raman spectroscopy, X-ray diffraction (XRD), X-ray photoelectron spectroscopy (XPS), energy dispersive X-ray spectroscopy (EDX), and high-resolution transmission electron microscopy (TEM) to characterize the crystals. The XRD analysis (Fig. 2a) was used to examine the crystallinity and crystal structure of the AgI nanoflakes. The distinct diffraction peaks at $2\theta$ values of 23.8° and 24.6° correspond closely to the characteristic diffraction peaks of the (002) and (101) crystal planes of AgI, confirming its typical hexagonal β-AgI phase (with dimensions of $a$ = 4.592 Å, $c$ = 7.510 Å, and a space group of $P6_3mc$) indexed to the JCPDS no. 09-0374.[22–24] The limited number of XRD peaks is indicative of a highly oriented crystal growth. This preferred orientation likely results from the confined-space CVD method combined with the templating effect of the underlying mica substrate. Mica offers atomically flat, pseudo-hexagonal basal planes that can guide the epitaxial alignment of overgrown crystals through van der Waals interactions. A similar behavior has been reported in systems such as $ReS_2$ and Ge films grown on mica, where XRD patterns also show only a few dominant reflections due to the anisotropic alignment of crystalline domains.[25,26]

Under ambient conditions, AgI typically exists as a two-phase mixture of the β (hexagonal wurtzite) and γ (cubic zinc blende) phases, depending on the synthesis conditions.[4,10,27] However, the XRD results indicate a pure β-AgI phase, suggesting that the CVD-grown flakes are structurally stable and compositionally uniform. Notably, the formation of pure β-AgI may result from the compression of tetragonal or rhombohedral AgI polymorphs during the growth process, as previously proposed.[21]

Two Raman modes are detected at 87 $cm^{-1}$ and 112 $cm^{-1}$ in the AgI samples (Fig. 2b). These modes correspond to the β-AgI polymorph and are attributed to its $E_2$ and $A_1$ modes, respectively. Similar Raman modes have been reported in the literature, though with slight shifts due to differences in the sample form and synthesis method. For example, Assis *et al.*[21] observed $E_2$ and $A_1$ modes at 83 $cm^{-1}$ and 103 $cm^{-1}$, respectively, in co-precipitated AgI powders containing mixed β- and γ-phases, and Cicconi *et al.*[28] reported comparable features in natural mineral samples. The upshifts in our CVD-grown single-crystalline nanoflakes to 87 $cm^{-1}$ and 112 $cm^{-1}$ can be attributed to internal strain, phonon confinement, and substrate interactions, which are known to influence vibrational frequencies in ultrathin crystalline materials.[29–31] These distinctions reflect the influence of crystal quality, morphology, and synthesis method on the Raman response of our β-AgI.

 

The elemental composition of the AgI crystals was analyzed by XPS. The binding energy scale was calibrated using the C 1s peak at 248.8 eV. The high-resolution XPS scan spectra for Ag 3d and I 3d are shown in Fig. 2c. The peaks located at 373.8 and 367.8 eV are attributed individually to Ag $3d_{3/2}$ and Ag $3d_{5/2}$, indicating the existence of $Ag^+$ in the as-grown sample.[22,24] The I 3d spectrum shows peaks at 630.3 eV and 618.8 eV, which are attributed to I $3d_{3/2}$ and I $3d_{5/2}$, respectively, confirming the presence of $I^-$ ions in AgI. Fig. S6 (ESI†) presents the Ag 3d XPS spectrum acquired after photo-induced degradation. Both the Ag $3d_{5/2}$ and Ag $3d_{3/2}$ peaks can be deconvoluted into two distinct components: the peaks at 367.7 eV and 373.8 eV correspond to $Ag^+$, while the additional peaks at 368.6 eV and 374.6 eV are assigned to metallic $Ag^0$. Similar spectral features have been reported by Cui *et al.*,[32] who observed the coexistence of $Ag^+$ and $Ag^0$ states in partially reduced silver-based systems. The appearance of $Ag^0$-related peaks provides clear evidence of partial reduction of $Ag^+$ to $Ag^0$, indicating the formation of metallic silver nanoparticles during the degradation process.

EDX analyses were carried out to verify the chemical compositions and purity of the AgI crystals. The EDX spectrum of the AgI crystal is depicted in Fig. 2d. The EDX spectrum indicates that the AgI nanostructure consists solely of Ag and I, with no impurities. The distribution of elements is confirmed through EDX elemental mapping. As illustrated in Fig. 2e, both the Ag and I elements are uniformly dispersed across the nanoflake. The oxygen background is obtained from the mica substrate.

### 2.3. Formation of Ag nanoparticles upon electron beam irradiation

During SEM imaging and EDX characterization, we observed degradation on the surface of the AgI crystals, accompanied by the formation of new features, similar to those seen in photo-induced degradation of nanoflakes at elevated temperatures. Fig. S7 (ESI†) illustrates the changes caused by exposure to electron beam irradiation. Specifically, Fig. S7b, d, and f (ESI†) depict the surface after one minute of electron beam exposure. Based on previous studies and our post-e-beam exposure analysis, we conclude that Ag nanoparticles are formed on the surface of the AgI crystals.[21] Furthermore, we observed that the number of Ag nanoparticles increased over time or with higher electron beam energy. This phenomenon is attributed to the progressive reduction of $Ag^+$ cations from the bulk to the surface, leading to the degradation of the material and the formation of a composite structure ($n$Ag/$Ag_{1-n}$I).

Fig. 3 presents the results for TEM measurements on AgI crystals. Low-magnification TEM images reveal the formation of Ag nanoparticles on the crystal surface following exposure to electron beam irradiation at 200 kV. The time required to generate these nanoparticles during TEM analysis is much shorter than that in SEM analysis, owing to the significantly higher acceleration voltages used for TEM imaging.[33] A high-resolution TEM image, depicted in Fig. 3e, highlights darker regions with distinct $d$-spacing values. Upon measuring these $d$-spacings, they are identified to be corresponding to the (111) crystal planes of the FCC crystal structure of Ag, aligned with

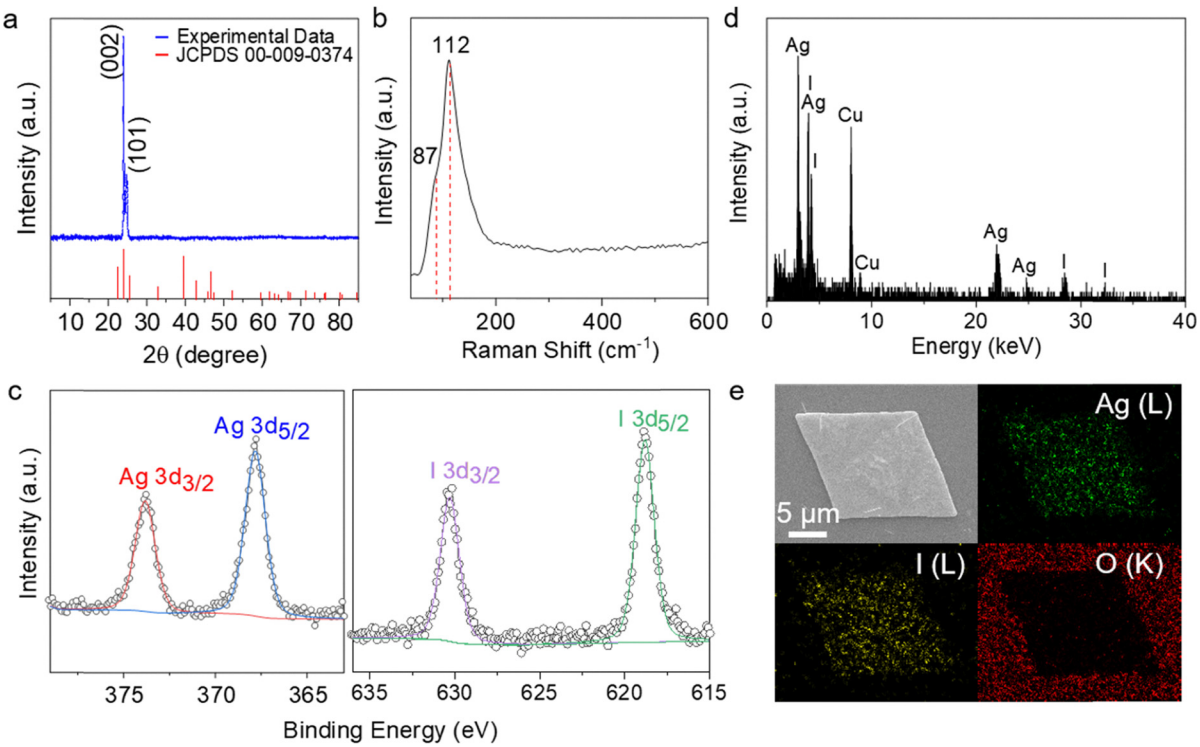


Fig. 2 (a) XRD $\theta$–$2\theta$ scan of the AgI crystals at room temperature. (b) Raman characterization of the AgI crystals. (c) XPS core-level regions of Ag 3d and I 3d, respectively. (d) EDX spectrum taken in TEM shows that Ag and I are the dominant elements. The traces of Cu are due to the TEM grid. (e) EDX maps of Ag, I, and O elements.

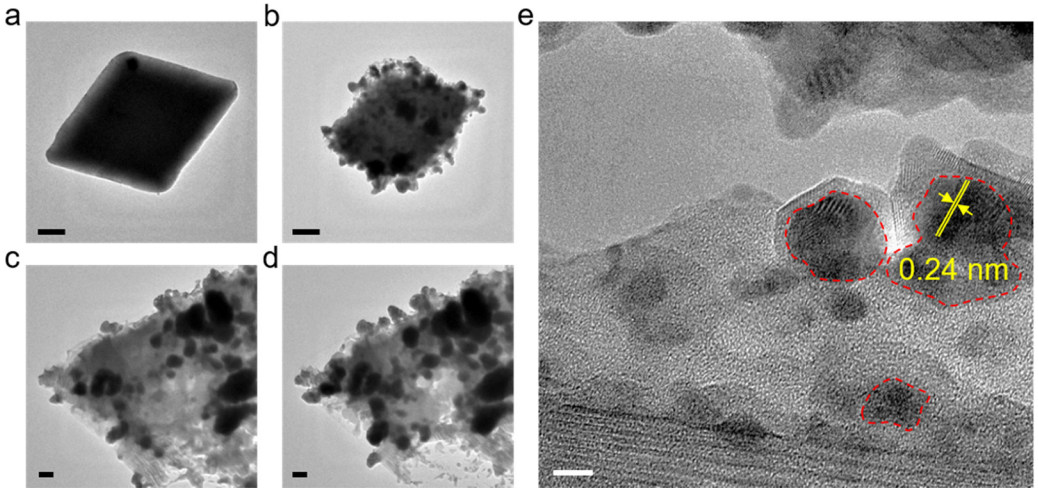


Fig. 3 TEM analysis of AgI crystals under electron beam irradiation at 200 kV. (a) Low-magnification image of an AgI crystal before degradation. (b) The same crystal after 20 seconds of irradiation, showing initial formation of Ag nanoparticles. The scale bar in (a) and (b) is 0.5 μm. (c) A second crystal after 1 minute of irradiation, exhibiting significant degradation and nanoparticle formation (black regions). (d) The same crystal from (c) after 5 seconds, highlighting the progression of degradation and expansion of Ag nanoparticles in certain regions. The scale bar in (c) and (d) is 0.1 μm. (e) High-resolution TEM image of degraded regions, showing dark areas with distinct *d*-spacing (0.24 nm) corresponding to the (111) planes of the Ag phase (JCPDS no. 04-0783). The red dashed areas show Ag nanoparticles. The scale bar is 5 nm.

JCPDS no. 04-0783.[34] This observation aligns with findings reported by Longo *et al.*,[33] confirming that electron beam irradiation induces the reduction of Ag within the AgI matrix, resulting in the formation of Ag nanoparticles.

AgI decorated with Ag nanoparticles has shown superior photocatalytic performance.[21,23,35] Yuan *et al.* reported enhanced photocatalytic activity of AgI under a broad solar spectrum, attributed to the presence of coexisting Ag nanoparticles.[35] Similarly, Wang *et al.* observed the partial formation of Ag nanoparticles alongside AgI, which induced characteristic surface plasmon resonance (SPR) effects and significantly improved the photocatalytic efficiency of Ag/AgI composites.[23] Developing one-pot methods to synthesize Ag/AgI plasmonic photocatalysts remains challenging, highlighting the need for new strategies to grow metallic Ag on AgI for advanced photocatalytic applications.

### 2.4. Device fabrication and electrical measurements

In earlier studies, AgI was employed as the switching medium to potentially construct electrochemical metallization (ECM) memristors, which rely on the formation and dissolution of metallic conductive filaments (CFs) under an electric field. ECM memristors show promise for memory and neuromorphic computing.[36,37] These devices typically use metal cations from an active electrode, like Ag, to create CFs, switching between low and high resistance states abruptly.[34] While traditional oxide-based ECM memristors face limitations in density and power efficiency, AgI might offer a promising alternative for high-performance, low-power memristors with fast switching and high integration potential. Here, we tested our single-crystalline samples for potential switching applications.

Top-silver-contacted device fabrication starts with the transferring of as-grown AgI nanoflakes on an $HfO_2$-coated $SiO_2$/Si substrate using the PMMA-assisted transferring method. In this method, the growth substrate is coated with a PMMA solution and baked at 170 °C for 5 minutes in the dark to prevent crystal degradation. The PMMA-coated sample is then placed in boiling water for 15 minutes and left to cool for 45 minutes. The film is removed from the growth substrate by wedging into water and transferred onto the $HfO_2$-coated $SiO_2$/Si substrate. Finally, the film is dissolved in acetone for 5 minutes, leaving the nanoflakes on the substrate. After dissolving the PMMA film, the nanoflakes are ready to be patterned using the Mask Aligner, followed by thermal evaporation of contacts, Cr (5 nm)/Ag (100 nm). The inset of Fig. 4a shows the top-silver-contacted device.

We examine how AgI conducts electricity at elevated temperatures (170 °C). The *I–V* curve reveals a transition from a high resistance state (HRS) to a low resistance state (LRS) at voltages exceeding ~0.9 V (Fig. 4a). Notably, applying a constant voltage of ~4 V results in a dramatic resistance drop of approximately six orders of magnitude (Fig. 4b). This behavior is likely due to the formation of conductive Ag nanowires bridging the electrodes, as observed in Fig. S8 (ESI†). EDX analysis was performed on the device, which was biased positively relative to the ground. The EDX maps reveal a depletion of silver in the source electrode (Fig. S8c, ESI†), consistent with $Ag^+$ ions migrating from the biased electrode toward the grounded terminal under the electric field.

When a voltage exceeding a certain threshold is applied, it can induce a liquid-like motion of $Ag^+$ ions within the nanoflake, with the electrodes acting as ion sources or sinks depending on the polarity. Fig. S9a (ESI†) shows another lateral device measured at high temperature, reproducing a similar switching behavior. The devices studied here showed signs of damage and did not exhibit reversible switching behavior. Further

 

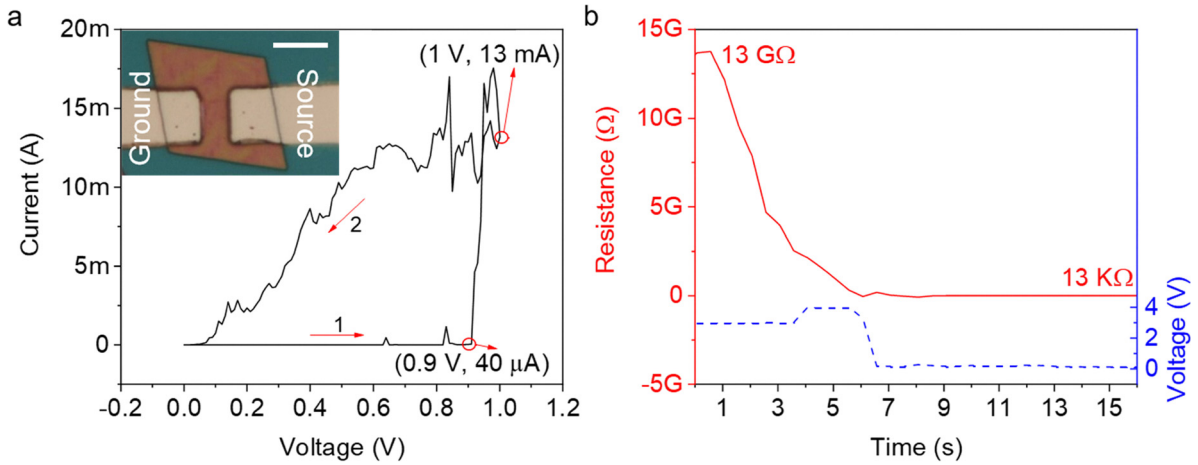


Fig. 4 (a) Output characteristics of a lateral Ag/AgI/Ag device measured at 170 °C, with an optical microscope image of the device shown in the inset. The scale bar is 10 μm. (b) Resistance as a function of time under varying applied voltages.

investigation on multiple devices is required to evaluate the reproducibility and reversibility of this behavior.

In addition to lateral configuration devices, AgI devices with a vertical configuration were also fabricated and measured. The process begins with patterning bottom electrodes on the substrate *via* photolithography, followed by thermal evaporation of 10 nm Cr/50 nm Ag and a lift-off process (Fig. 5a). The choice of metal contact and electrode design plays a critical role in ensuring reliable device performance. As reported by Malureanu *et al.*,[38] when the Ag thickness exceeds approximately 10 nm, the deposited film becomes continuous, thereby reducing contact resistance. Furthermore, Bahari *et al.*[39] demonstrated that interface engineering during metal deposition can effectively suppress leakage currents and enhance contact stability.

AgI nanosheets grown on a mica substrate are then transferred using a wet transfer method, similar to the PMMA-assisted technique described earlier, but with an additional step. Instead of being placed directly onto the target substrate, the detached film is first transferred onto PDMS. This intermediate step allows precise alignment of the nanosheet with the pre-patterned electrodes, ensuring proper placement over the electrode channel. Before bringing the PDMS-supported film into contact with the substrate, a droplet of acetone is applied to the substrate, followed by heating to 50 °C. This facilitates the release of the film from PDMS onto the substrate. The subsequent steps follow the same procedure as the PMMA-assisted transfer method described earlier. Finally, the top electrode is patterned using a mask aligner after aligning the crystal with the mask pattern, followed by 10 nm Cr/100 nm Ag deposition *via* thermal evaporation and lift-off. Fig. 5b illustrates the vertical-configuration device using silver contacts.

Fig. 5c shows the *I*–*V* characteristic of the device, where the voltage is swept from 0 to +5 V, back to 0, then to −5 V, and finally returned to 0 V. Large hysteresis windows are evident in both the positive and negative voltage ranges.

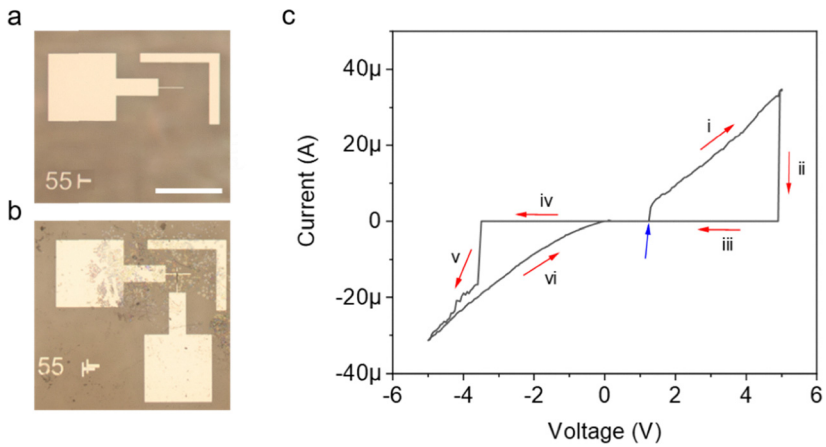


Fig. 5 (a) A 10 nm Cr/50 nm Ag deposited contact on an empty sapphire substrate. (b) Optical image of the AgI device in a vertical configuration after transferring AgI crystals onto the pre-patterned Ag bottom electrode, followed by patterning and depositing 10 nm Cr/100 nm Ag as the top electrode. The scale bar is 300 μm. (c) *I*–*V* cycles of symmetric AgI devices with Ag contacts in a vertical configuration. The *I*–*V* cycle shows large hysteresis windows, exhibiting memristive behavior. The blue arrow points to the forming voltage at 1.25 V. The red arrows indicate the sweep direction.

Specifically, the device exhibits memristive behavior, with a forming
voltage around 1.25 V. A transition from LRS to HRS occurs at a RESET voltage near +5 V, while in the negative bias range, a transition from HRS to LRS is observed at the SET voltage of approximately −3.5 V. Fig. S9b (ESI†) presents another vertical device with similar hysteresis window, suggesting memristive behavior.

The resistive switching behavior in the vertical Ag/AgI/Ag devices is likely governed by field-driven migration of $Ag^+$ ions and subsequent filament formation between the two active silver electrodes,[34,40] consistent with the drift-controlled SET and diffusion-controlled RESET mechanisms proposed by Wang *et al.*[41] Additionally, factors such as crystal thickness and current compliance can significantly influence filament stability and retention.[42] Further investigation of these parameters in AgI-based devices would be valuable for understanding filament evolution dynamics and optimizing switching performance.

## 3. Conclusions

In conclusion, we have demonstrated the synthesis of single-crystalline AgI flakes *via* confined-space CVD under real-time optical observation. We have shown that AgI crystals are highly oriented along the crystal's symmetry axis and are in the β-phase at room temperature. The marked sensitivity to light and electron beam exposure, especially above the phase transition temperature, is studied in depth. Our results show the formation of Ag nano-islands on the surface and within the crystals upon irradiation. Two-terminal devices of lateral and vertical geometries exhibit a large, ionic-based switching upon application of a voltage bias. The unique combination of facile synthesis, sharp conductivity transitions, and intrinsic memristive capabilities positions thin single-crystalline AgI as a promising candidate for application in next-generation electronics.

## Author contributions

AP performed the crystal synthesis, characterization, and electrical measurements, with the assistance of AAS, DP, HMS, and EY. TSK conceded the project and guided the experiments. AP wrote the draft, and all authors contributed to the writing of the manuscript.

## Conflicts of interest

There are no conflicts to declare.

## Data availability

The data that support the plots within this paper and other findings of this study are available from the corresponding authors upon request. A part of data supporting this article has been included in the ESI.†

## Acknowledgements

T. S. K. acknowledges funding from TUBITAK under grant #121F366.

## References

1 J. B. H. Boyce and B. A. Huberman, *Phys. Rep.*, 1979, **51**, 189–265.
2 D. A. Keen, S. Hull, W. Hayes and N. J. G. Gardner, *Phys. Rev. Lett.*, 1996, **77**, 4914.
3 A. J. E. Rettie, J. Ding, X. Zhou, M. J. Johnson, C. D. Malliakas, N. C. Osti, D. Y. Chung, R. Osborn, O. Delaire, S. Rosenkranz and M. G. Kanatzidis, *Nat. Mater.*, 2021, **20**, 1683–1688.
4 D. A. Keen, S. Hull, A. C. Barnes, P. Berastegui, W. A. Crichton, P. A. Madden, M. G. Tucker and M. Wilson, *Phys. Rev. B*, 2003, **68**, 014117.
5 S. J. Lee, Z. Lin, J. Huang, C. S. Choi, P. Chen, Y. Liu, J. Guo, C. Jia, Y. Wang, L. Wang, Q. Liao, I. Shakir, X. Duan, B. Dunn, Y. Zhang, Y. Huang and X. Duan, *Nat. Electronics*, 2020, **3**, 630–637.
6 N. Ahmad, A. M. Alshehri, Z. R. Khan, I. Ahmad, P. M. Z. Hasan, A. A. Melaibari and M. Shkir, *Mater. Sci. Semicond. Process.*, 2022, **137**, 106239.
7 A. E. Lukin, E. N. Ivanova, S. V. Pan'kova, V. G. Solovyev and V. L. Veisman, *J. Phys.: Conf. Ser.*, 2014, **572**, 012047.
8 Y. Mateyshina, D. Alekseev and N. Uvarov, *Mater. Today: Proc.*, 2020, **25**, 373–376.
9 T. Yamamoto, M. Maesato, N. Hirao, S. I. Kawaguchi, S. Kawaguchi, Y. Ohishi, Y. Kubota, H. Kobayashi and H. Kitagawa, *J. Am. Chem. Soc.*, 2017, **139**, 1392–1395.
10 T. Takahashi, *J. Appl. Electrochem.*, 1973, **3**, 79–90.
11 M. Y. Ma, N. K. Chen, D. Wang, D. Han, H.-B. Sun, S. Zhang and X.-B. Li, *Mater. Today Nano*, 2023, **22**, 100304.
12 M. C. Lucking, W. Xie, D. H. Choe, D. West, T. M. Lu and S. B. Zhang, *Phys. Rev. Lett.*, 2018, **120**, 086101.
13 M. Y. Ma, D. Han, N. K. Chen, D. Wang and X. B. Li, *Materials*, 2022, **15**, 7715.
14 B. V. Andryushechkin and T. V. Pavlova, *J. Chem. Phys.*, 2022, **156**, 164702.
15 H. R. Rasouli, N. Mehmood, O. Cakiroglu and T. S. Kasirga, *Nanoscale*, 2019, **11**, 7317–7323.
16 H. R. Rasouli, N. Mehmood, O. Çakiroglu, E. C. Sürmeli and T. S. Kasirga, *Phys. Rev. B*, 2019, **100**, 161107.
17 H. R. Rasouli, J. Kim, N. Mehmood, A. Sheraz, M. K. Jo, S. Song, K. Kang and T. S. Kasirga, *Nano Lett.*, 2021, **21**, 3997–4005.
18 A. Parsi, A. A. Suleiman, M. Razeghi, D. Pehlivanoglu, O. Oguz, U. Basci, H. M. Shakir, E. Yegin and T. S. Kasirga, *Nanoscale*, 2025, **17**, 9337–9345.

 

19 R. Somphonsane, T. Chiawchan, W. Bootsa-Ard and H. Ramamoorthy, *Materials*, 2023, **16**, 4817.
20 A. Borchers and T. Pieler, *Genes*, 2010, **1**, 413–426.
21 M. Assis, F. C. Groppo Filho, D. S. Pimentel, T. Robeldo, A. F. Gouveia, T. F. D. Castro, H. C. S. Fukushima, C. C. de Foggi, J. P. C. da Costa, R. C. Borra, J. Andrés and E. Longo, *ChemistrySelect*, 2020, **5**, 4655–4673.
22 C. Ye, F. Xu, Z. Wu, Z. F. Gao and M. Wang, *Nanotechnology*, 2021, **32**, 445501.
23 N. Wang, Y. Xing, S. Song, J. Liu, H. Xia, F. Tian, G. Xu, Z. Ren and P. Chen, *Appl. Surf. Sci.*, 2024, **654**, 159521.
24 Z. Jiao, Z. Liu and Z. Ma, *ACS Omega*, 2019, **4**, 7919–7930.
25 J. K. Qin, W.-Z. Shao, Y. Li, C.-Y. Xu, D.-D. Ren, X.-G. Song and L. Zhen, *RSC Adv.*, 2017, **7**, 24188–24194.
26 A. J. Littlejohn, Y. Xiang, E. Rauch, T. M. Lu and G. C. Wang, *J. Appl. Phys.*, 2017, **122**, 185305.
27 A. S. Awed, G. S. El-Sayyad, A. El-ghandour, M. F. O. Hameed, M. I. A. Abdel Maksoud, A. I. El-Batal and S. S. A. Obayya, *J. Cluster Sci.*, 2019, **32**, 1–16.
28 M. R. Cicconi, E. Pili, L. Grousset, P. Florian, J. C. Bouillard, D. Vantelon and D. R. Neuville, *Sci. Rep.*, 2019, **9**, 7758.
29 Y. Zhao, X. Luo, H. Li, J. Zhang, P. T. Araujo, C. K. Gan, J. Wu, H. Zhang, S. Y. Quek, M. S. Dresselhaus and Q. Xiong, *Nano Lett.*, 2013, **13**, 1007–1015.
30 P. H. Tan, W. P. Han, W. J. Zhao, Z. H. Wu, K. Chang, H. Wang, Y. F. Wang, N. Bonini, N. Marzari, N. Pugno, G. Savini, A. Lombardo and A. C. Ferrari, *Nat. Mater.*, 2012, **11**, 294–300.
31 X. Zhang, X. F. Qiao, W. Shi, J. B. Wu, D. S. Jiang and P. H. Tan, *Chem. Soc. Rev.*, 2015, **44**, 2757–2785.
32 D. H. Cui, Y. F. Zheng and X. C. Song, *J. Alloys Compd.*, 2017, **701**, 163–169.
33 E. Longo, L. S. Cavalcante, D. P. Volanti, A. F. Gouveia, V. M. Longo, J. A. Varela, M. O. Orlandi and J. Andres, *Sci. Rep.*, 2013, **3**, 1676.
34 C. Li, T. Xu, R. Pan, S. Bao, K. Yin, J. Shen, Y. Zhu, S. Hou and L. Sun, *ACS Nano*, 2024, **18**, 32196–32204.
35 X. Yuan, Z. Wu, G. Zeng, L. Jiang, J. Zhang, T. Xiong, H. Wang and D. Mo, *Appl. Surf. Sci.*, 2018, **454**, 293–304.
36 Y. Zhang, G. Q. Mao, X. Zhao, Y. Li, M. Zhang, Z. Wu, W. Wu, H. Sun, Y. Guo, L. Wang, X. Zhang, Q. Liu, H. Lv, K. H. Xue, G. Xu, X. Miao, S. Long and M. Liu, *Nat. Commun.*, 2021, **12**, 7232.
37 S. J. Yang, Y.-R. Jeon, D. Kim, S. Mohan, S. Kutagulla, M. Disiena, S. K. Banerjee and D. Akinwande, *npj 2D Mater. Appl.*, 2025, **9**, 9.
38 R. Malureanu and A. Lavrinenko, *Nanotechnol. Rev.*, 2015, **4**, 259–275.
39 A. Bahari, *J. Mater. Sci.: Mater. Electron.*, 2024, **35**, 1709.
40 S. J. Kim, I. H. Im, J. H. Baek, S. H. Park, J. Y. Kim, J. J. Yang and H. W. Jang, *ACS Nano*, 2024, **18**, 28131–28141.
41 W. Wang, E. Covi, Y.-H. Lin, E. Ambrosi, A. Milozzi, C. Sbandati, M. Farronato and D. Ielmini, *IEEE Trans. Electron Devices*, 2021, **68**, 4342–4349.
42 E. Covi, W. Wang, Y.-H. Lin, M. Farronato, E. Ambrosi and D. Ielmini, *IEEE Trans. Electron Devices*, 2021, **68**, 4335–4341.